

Electrical tuning of magnetism in Fe₃O₄/PZN–PT multiferroic heterostructures derived by reactive magnetron sputtering

Ming Liu,¹ Ogheneyunume Obi,¹ Zhuhua Cai,² Jing Lou,¹ Guomin Yang,¹
Katherine S. Ziemer,² and Nian X. Sun^{1,a)}

¹*Department of Electrical and Computer Engineering, Northeastern University, Boston, Massachusetts 02115, USA*

²*Department of Chemical Engineering, Northeastern University, Boston, Massachusetts 02115, USA*

(Received 31 August 2009; accepted 3 February 2010; published online 15 April 2010)

Strong magnetoelectric (ME) coupling was demonstrated in Fe₃O₄/PZN–PT (lead zinc niobate–lead titanate) multiferroic heterostructures obtained through a sputter deposition process. The dependence of the magnetic anisotropy on the electric field (E-field) is theoretically predicted and experimentally observed by ferromagnetic resonance spectroscopy. A large tunable in-plane magnetic anisotropy of up to 600 Oe, and tunable out-of-plane anisotropy of up to 400 Oe were observed in the Fe₃O₄/PZN–PT multiferroic heterostructures, corresponding to a large ME coefficient of 100 Oe cm/kV in plane and 68 Oe cm/kV out of plane, which match well with predicted results. In addition, the electric field manipulation of magnetic anisotropy is also demonstrated by the electric fields dependence of magnetic hysteresis loops, showing a large squareness ratio change of 44%. These Fe₃O₄/PZN–PT multiferroic heterostructures exhibiting large E-field tunable magnetic properties provide great opportunities for novel electrostatically tunable multiferroic devices. © 2010 American Institute of Physics. [doi:10.1063/1.3354104]

I. INTRODUCTION

Electric field (E-field) tuning of magnetism has become an exciting new frontier due to its wide range of potential applications in information storage, sensors, and novel electrostatically tunable microwave magnetic devices such as filters, resonators, inductors, and phase shifters.^{1–9} Multiferroic composites consisting of ferro/ferrimagnetic and ferroelectric phases are widely recognized to be able to realize electric field control of magnetic order due to its strong strain mediated magnetoelectric (ME) coupling resulting from the inverted piezoelectric effect and piezomagnetic effect.^{10–19} Several multiferroic heterostructures have been known to show large electrical field manipulation of magnetism, such as FeGaB/Si/PMN–PT (lead magnesium niobate–lead titanate), yttrium iron garnet (YIG)/PMN–PT and YIG/BSTO (barium strontium titanate),^{8,10,11,20,21} which show great prospects for E-field tunable magnetic devices. However, the tunable ranges of most demonstrated microwave multiferroic devices are still quite limited.^{9,19,20}

Recently, we reported a giant electric field tuning of magnetic anisotropy in layered multiferroic heterostructures derived by a wet chemical spin-spray process at 90 °C, showing a large electric field tuning of ferromagnetic resonance (FMR) field up to 600 Oe in Fe₃O₄/PMN–PT at microwave frequency, corresponding to a ME coefficient of 67 Oe cm/V, and displaying potential applications for microwave tunable devices.²² In this work, an alternative growth method of reactive magnetron sputtering was employed to deposit crystalline magnetite film on (011) cut single crystal PZN–PT at room temperature. Large tunable ranges of in-plane FMR field of up to 600 Oe and out-of-

plane FMR field of up to 400 Oe were observed, corresponding to high ME coupling coefficients of 100 Oe cm/kV and 68 Oe cm/kV, respectively. Compared to spin-spray derived Fe₃O₄/PMN–PT, magnetron sputtering could deliver high quality Fe₃O₄ film with high uniformity, low surface roughness, and high reproducibility.

II. EXPERIMENTAL

Fe₃O₄ thin films were deposited on amorphous glass substrates and (011) cut single crystal PZN–PT substrates by reactive sputtering iron (DC) target in argon and oxygen mixture atmosphere at room temperature. Glass and PZN–PT substrates were cleaned by sequentially rinsing in acetone and ethanol solutions. Before deposition, the chamber was pumped to below 1×10^{-7} Torr. The deposition process was performed at room temperature in an Ar+O₂ mixture gas environment with a pressure of 3 mTorr at a power density of 5 W/cm². Crystal structures and composition of Fe₃O₄ films were characterized by x-ray diffraction (XRD) with a Cu K_α source ($\lambda = 1.541 \text{ \AA}$), x-ray photoelectron spectroscopy (XPS), scanning electron microscope (SEM), and atomic force microscope (AFM). Magnetic properties of the Fe₃O₄ film and ME coupling measurement in Fe₃O₄/PZN–PT were performed by vibrating sample magnetometer (VSM) and x-band electron paramagnetic resonance (EPR) system.

III. RESULTS AND DISCUSSION

Figure 1(a) shows the XRD patterns of the iron-oxide films on glass and PZN–PT substrates deposited at room temperature with different oxygen flow rates. A narrow range of oxygen flow rates between 0.25–0.28 SCCM (SCCM denotes standard cubic centimeter per minute at STP) was determined to form pure polycrystalline Fe₃O₄ phase at a fixed

^{a)}Electronic mail: nian@ece.neu.edu.

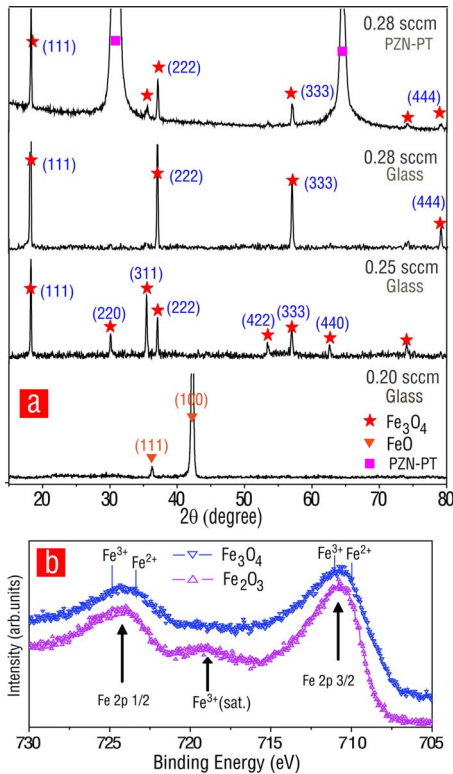


FIG. 1. (Color online) (a) XRD patterns of Fe–O films on glass and PZN–PT substrates with different oxygen flow rates and (b) XPS spectra of Fe₃O₄/glass (top curve) and Fe₂O₃/glass (bottom curve) when oxygen flow rates were 0.28 and 0.40 SCCM, respectively.

argon flow rate of 20 SCCM. In particular, when oxygen flow rate reaches 0.28 SCCM, the Fe₃O₄ film exhibits a highly preferred (111) texture on both glass and PZN–PT substrates. XPS analyses were carried out to further confirm the magnetite Fe₃O₄ phase in the films. As shown in Fig. 1(b), core-level XPS spectra confirms that the deposited film grown with the oxygen flow rate of 0.28 SCCM is Fe₃O₄, which has broad Fe 2*p* peaks. The broad peaks for the Fe₃O₄ are attributed to the existence of dual iron oxidation states (Fe²⁺ and Fe³⁺) that have different, but nonresolvable binding energies, indicating the pure Fe₃O₄ thin film. In contrast, the Fe 2*p* spectrum for the Fe₂O₃ phase derived with a high oxygen flow rate of 0.40 SCCM shows narrow peaks and a shake-up satellite peak at ~719 eV, which is the characteristic of pure Fe³⁺ in Fe₂O₃. There might be interdiffusion between the film and substrate, however, since Fe₃O₄ is grown on PZN–PT at room temperature, interdiffusion, if any, should be minimized. We will carry out cross-section TEM measurement interface analysis in the future.

The surface and cross-section SEM images for the Fe–O films obtained at different oxygen flow rates are shown in Fig. 2. Clearly, typical columnar grains with the diameter of 50–100 nm can be observed for the Fe₃O₄ film with a (111) texture, which was grown with an oxygen flow rate of 0.28 SCCM. Larger grains are observed at an oxygen flow rate of 0.25 SCCM, which is related to a polycrystalline Fe₃O₄ phase without obvious texture. The film thickness was determined to be 800 nm from the cross-section SEM [Fig. 2(c)].

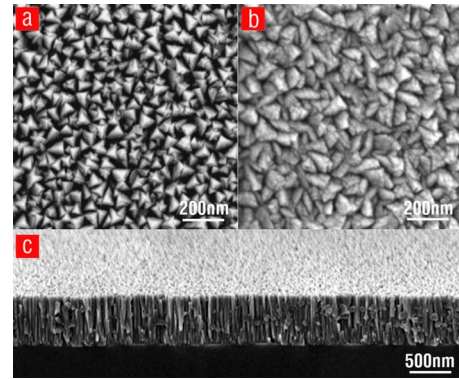


FIG. 2. (Color online) Top view SEM images of Fe₃O₄/glass with different oxygen flow rate of (a) 0.28 SCCM and (b) 0.25 SCCM and (c) cross-section SEM image of Fe₃O₄/glass.

In addition, the Fe₃O₄ film displayed a smooth surface with the roughness of 4 nm determined by AFM.

Magnetic hysteresis loops of the reactive sputtering derived multiferroic composite Fe₃O₄/PZN–PT were measured by VSM. Well-defined magnetic hysteresis loops were observed when an external magnetic field was applied parallel or perpendicular to the film plane, showing an in-plane coercivity of 116 Oe and an out-of-plane coercivity of 85 Oe, respectively. The saturation magnetization of Fe₃O₄ film was determined to be 420 ± 10 emu/cm³.

Imposing an electric field induced a strain on the piezoelectric phase leads to a stress on the magnetic phase through ME coupling. In a multiferroic heterostructure shown in Fig. 3(a), an applied electric field in the piezoelectric phase produces biaxial in-plane stresses in the magnetic phase σ_x, σ_y , which can be isotropic ($\sigma_x = \sigma_y$) or anisotropic ($\sigma_x \neq \sigma_y$). The magnetoelastic energy contribution can be expressed as

$$F_{me} = -\frac{3}{2}\lambda\sigma_x \sin^2 \theta \cos^2 \phi - \frac{3}{2}\lambda\sigma_y \sin^2 \theta \sin^2 \phi,$$

where θ, ϕ are angles defined as shown in Fig. 3(a) and λ is the in-plane effective magnetostriction coefficient for the magnetic phase (i.e., textured polycrystalline Fe₃O₄ magnetic film in our experiments). The energy surfaces were plotted in Fig. 3 for several special cases of the stress magnetostriction products ($\lambda\sigma$). To accommodate the electric field induced biaxial stress in three dimensions, the magnetization seeks the lowest energy orientation on energy surface. For example, when $\lambda\sigma_x = \lambda\sigma_y > 0$, the lowest magnetoelastic energy is obtained at $z=0$ plane, as shown in Fig. 3(b), indicating that magnetization of the magnetic film tends to stay in the magnetic film plane; In contrast, when $\lambda\sigma_x = \lambda\sigma_y < 0$, a magnetic easy axis is formed along z direction as shown in Fig. 3(c). In addition, for anisotropic biaxial stresses (for example $\lambda\sigma_x < 0, \lambda\sigma_y > 0$ in single crystal PZN–PT), $y=0$ becomes easy plane as shown in Fig. 3(d).

This electric field induced biaxial stresses not only redistribute the free energy but also produce the effective anisotropy field \vec{H}_{eff} which is defined as a negative gradient of magnetoelastic energy on magnetization vector: $\vec{H}_{\text{eff}} = -\nabla_{\vec{M}} F_{\text{ME}}$. By this definition, the total energy under the external magnetic field \vec{H} can be expressed as $F_{\text{total}} = F_{\text{ME}}$

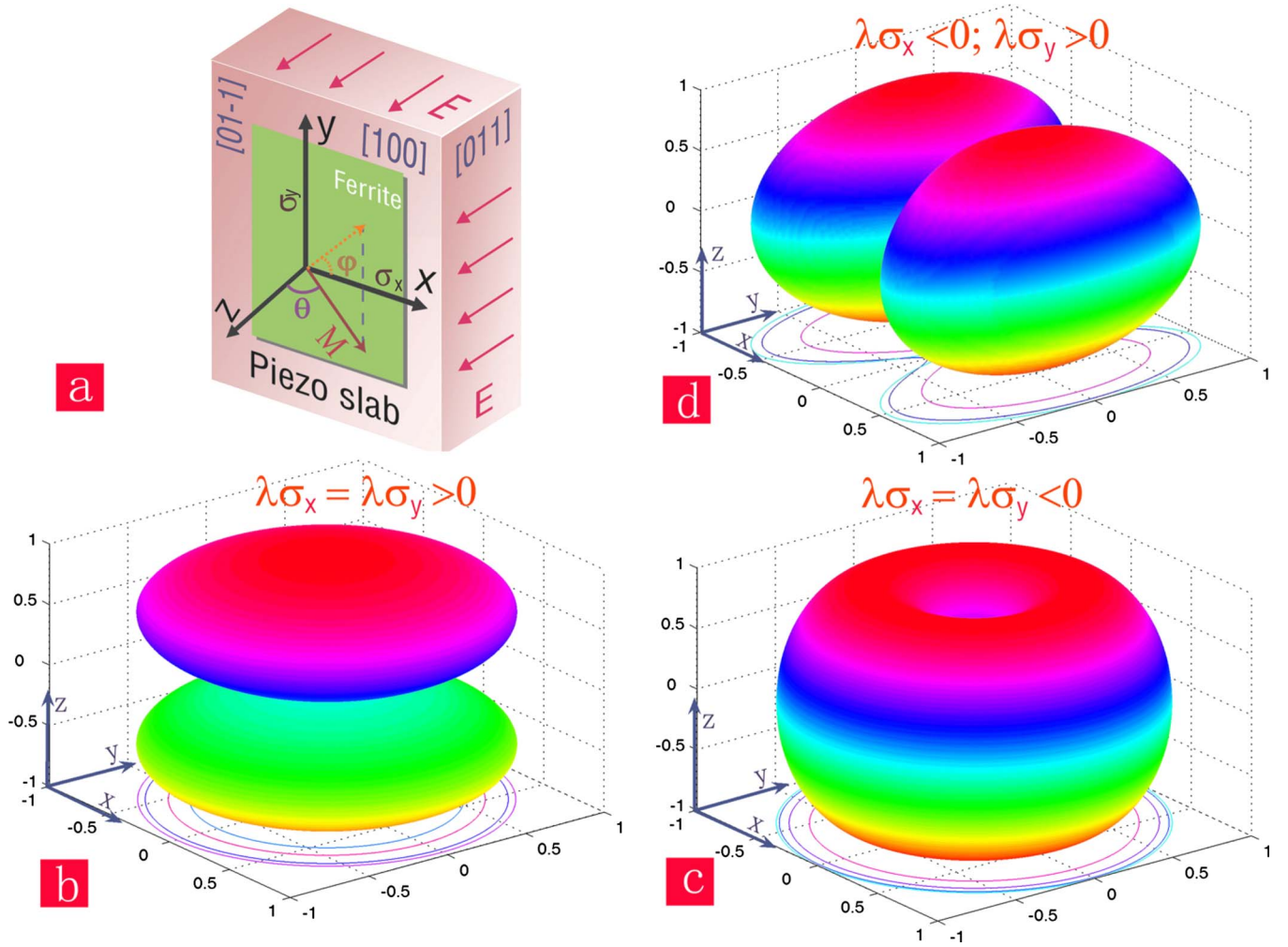


FIG. 3. (Color online) (a) Schematic of laminate multiferroic $\text{Fe}_3\text{O}_4/\text{PZN-PT}$ and [(b)–(d)] the electric field induced magnetoelastic energy surface.

$-\vec{H} \cdot \vec{M}_s = -(\vec{H}_{\text{eff}} + \vec{H}) \cdot \vec{M}_s$, in which the contribution of magnetoelastic energy is equivalent to applying a effective anisotropy field \vec{H}_{eff} . Given the free energy that incorporates the Zeeman energy and shape anisotropy, we have

$$F_{\text{free}} = F_{\text{ME}} + F_{\text{zeeman}} = -\frac{3}{2}\lambda\sigma_x \sin^2 \theta \cos^2 \phi - \frac{3}{2}\lambda\sigma_y \sin^2 \theta \sin^2 \phi - \vec{H} \cdot \vec{M}_s + 2\pi M_s \cos^2 \theta.$$

The magnitude of effective anisotropy field \vec{H}_{eff} can be determined by

$$\begin{cases} H_{\text{eff},\theta,\varphi_0} = \frac{1}{M_s} \left. \frac{\partial^2 F_{\text{me}}}{\partial \theta^2} \right|_{\theta=\theta_0+\Delta\theta, \varphi=\varphi_0} \\ H_{\text{eff},\theta_0,\varphi} = \frac{1}{M_s} \left. \frac{\partial^2 F_{\text{me}}}{\partial \varphi^2} \right|_{\theta=\theta_0, \varphi=\varphi_0+\Delta\varphi} \end{cases}$$

, where, θ_0, φ_0 are derived from the first derivative of free energy equal to zero, and $\Delta\theta, \Delta\varphi$ are angles deviating from θ_0, φ_0 . So the in-plane biaxial stresses induced effective anisotropy along various axis are as follows:

$$H_{\text{eff},x} = \frac{3\lambda(\sigma_x - \sigma_y)}{M_s}, \quad H_{\text{eff},y} = \frac{-3\lambda(\sigma_x - \sigma_y)}{M_s},$$

$$H_{\text{eff},z} = \frac{-3\lambda(\sigma_x + \sigma_y)}{M_s}.$$

In our case, (011) cut single crystal PZN-PT displays large anisotropic in-plane piezoelectric coefficients of d_{31} (-3000 pC/N) and d_{32} (1000 pC/N), which could generate in-plane compressive stress σ_x along $[100]$ (d_{31}) direction and tensile stress σ_y along $[01\bar{1}]$ (d_{32}) direction under an electric field E parallel to $[011]$ (d_{33}) direction. Considering Hooke's law for plane stress, these stresses can be described by

$$\begin{pmatrix} \sigma_x \\ \sigma_y \end{pmatrix} = \frac{Y}{1-\nu^2} \begin{pmatrix} 1 & \nu \\ \nu & 1 \end{pmatrix} \begin{pmatrix} d_{31} \\ d_{32} \end{pmatrix} E.$$

So, the electric field induced effective magnetic field H_{eff} along different direction and its corresponding ME coupling coefficient $\alpha_{\text{ME}} = H_{\text{eff}}/E$ can be expressed by

$$\left\{ \begin{array}{l} H_{\text{eff},x} = \frac{3\lambda Y}{M_s(1+\nu)}(d_{31} - d_{32})E; \quad \alpha_{\text{ME},x} = \frac{3\lambda Y}{M_s(1+\nu)}(d_{31} - d_{32}) \\ H_{\text{eff},y} = \frac{-3\lambda Y}{M_s(1+\nu)}(d_{31} - d_{32})E; \quad \alpha_{\text{ME},y} = \frac{-3\lambda Y}{M_s(1+\nu)}(d_{31} - d_{32}) \\ H_{\text{eff},z} = \frac{-3\lambda Y}{M_s(1+\nu)}(d_{31} + d_{32})E; \quad \alpha_{\text{ME},z} = \frac{-3\lambda Y}{M_s(1+\nu)}(d_{31} + d_{32}) \end{array} \right. , \quad (1)$$

where, Y is the Young's Modulus of Fe_3O_4 (2.3×10^{12} dyne/cm²), ν is the Poisson's ratio of 0.26,²³ and E is the applied external electrical field. Since the Fe_3O_4 film has a preferred [111] orientation and shows an isotropic in plane, the magnetostriction constant λ should be the in-plane integration, which is estimated to be $\sim 20 \times 10^{-6}$. Considering an electric field of 6 kV/cm is applied, the calculated effective magnetic fields are

$$H_{\text{eff},x} = -640 \text{ Oe}; \quad H_{\text{eff},y} = 640 \text{ Oe}; \quad H_{\text{eff},z} = 320 \text{ Oe}. \quad (2)$$

The electric field induced effective magnetic field can be quantitatively determined by measuring in-plane and out-of-plane FMR field, which can be expressed by Kittel equations for both in-plane and out-of-plane cases

$$\text{In-plane: } f = \gamma \sqrt{(H_r + H_{\text{eff}})(H_r + H_k + H_{\text{eff}} + 4\pi M_s)},$$

$$P \propto \frac{\gamma^2 \sqrt{(H_a + H_k + H_{\text{eff}})(H_a + H_k + H_{\text{eff}} + 4\pi M_s)} 4\pi M_s \alpha}{[\gamma \sqrt{(H_a + H_k + H_{\text{eff}})(H_a + H_k + H_{\text{eff}} + 4\pi M_s)} - f_0]^2 + (f_0 \alpha)^2}, \quad (3)$$

where f_0 is working frequency of 9.3 GHz and α is Gilbert damping constant.²⁴

As shown in Fig. 4(a), a large electric-field induced FMR field upward shift of 600 Oe was observed when magnetic fields were applied along [100] (d_{31}) direction, corresponding to an average magnetoelectric coupling coefficient of 100 Oe cm/kV. This FMR field upward shift may be as a result of a negative $H_{\text{eff},x}$ in Eq. (1) which leads to increased H_r in Eq. (2). It is notable that the measured value of $H_{\text{eff},x} = -600$ Oe is very close to the predicted result of -640 Oe as shown in Eq. (2). When the magnetic field was applied along the $[0\bar{1}1]$ (d_{32}) direction, a downward shift in the FMR field ($H_{\text{eff},y}$) of up to 600 Oe was achieved, which was also close to the calculated value of 640 Oe, as shown in Fig. 4(b). In addition, a large out-of-plane FMR field downward shift of 400 Oe was also observed, leading to a positive $H_{\text{eff},z}$. Considering the upward and downward shifts of in-

$$\text{Out-of-plane: } f = \gamma(H_r + H_k + H_{\text{eff},z} - 4\pi M_s),$$

where f is frequency in megahertz, γ is the gyromagnetic ratio of 2.8 MHz/Oe, H_r is the resonance field supplied by an external electromagnet, H_k is the in-plane magnetic anisotropy, and H_{eff} is the in-plane effective magnetic anisotropy which would be $H_{\text{eff},x}$ or $H_{\text{eff},y}$ depending upon the external magnetic field direction. By observing the change in resonance field H_r at different electrical fields, the electric field induced effective magnetic field H_{eff} and their ME coupling coefficients can be quantitatively determined.

In our experiments, an x-band (9.3 GHz) EPR system was used for FMR measurements. The sample was placed in a rectangular cavity working at TE_{102} mode. External magnetic fields were sequentially applied along the [100], $[0\bar{1}1]$, and [011] direction of the (011) cut PZN-PT substrate while an external electric fields was applied across the thickness direction varying from 0 to 6 kV/cm. As the external magnetic field is varied through resonance field, the absorbed microwave energy in cavity is proportional to the image part of magnetic susceptibility, which was ideally expressed by

plane FMR fields due to anisotropic in-plane piezoelectric coefficients of PZN-PT, the electric field induced FMR tunable range can be significantly enhanced to 970 Oe by switching the external magnetic field direction with respect to the crystallographic orientation of the (011) cut PZN-PT, as shown in Fig. 4(d).

Combining Eqs. (1)–(3), the FMR spectra at different electric fields can be theoretically derived and compared with normalized experimental results as shown in Fig. 5 for the case when the external magnetic field is applied along [100] direction. Well-fitted FMR spectrum (dashed line) was obtained at external electric field of 0 kV/cm with damping constant of 0.165. Increasing the applied electric field to 6 kV/cm, the fitted FMR spectrum is shifted up by 640 Oe, which is consistent with the experimental result (solid line) and close to the tunable FMR range of 600 Oe.

The hysteresis loops of the $\text{Fe}_3\text{O}_4/\text{PZN-PT}$ heterostruc-

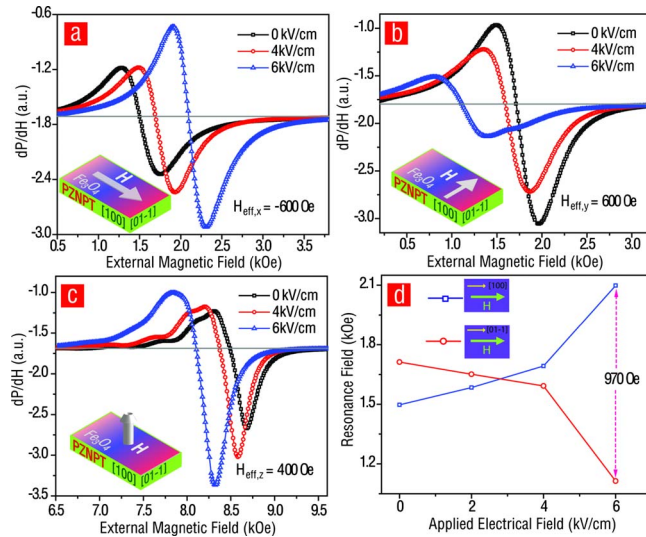


FIG. 4. (Color online) FMR absorption spectra at different electric fields while the external magnetic fields was applied along (a) [100], (b) [011], and (c) [011] directions of PZN-PT.

ture were also measured at different electric fields. As shown in Fig. 6(a), when an external magnetic field was applied along [100] direction, the magnetization process of the $\text{Fe}_3\text{O}_4/\text{PZN-PT}$ became harder and displayed a reduction in squareness ratio with 44% as increasing electric fields. This is because of a negative magnetic anisotropy which is produced by the combination of an electric field induced compressive stress and a positive magnetostriction constant of Fe_3O_4 . In contrast, an opposite trend of hysteresis loop dependence of electric field was observed when external magnetic field was along [011] direction due to the electric field induced tensile stress as shown in Fig. 6(b).

IV. SUMMARY

In summary, strong electric field tuning of magnetism in magnetron sputtering derived $\text{Fe}_3\text{O}_4/\text{PZN-PT}$ has been theoretically investigated and experimentally demonstrated. The experimental results showed a giant tunable magnetic anisotropy range of 600 Oe for in plane and 400 Oe for out-of-plane, corresponding to large ME coefficients of 100 and 68

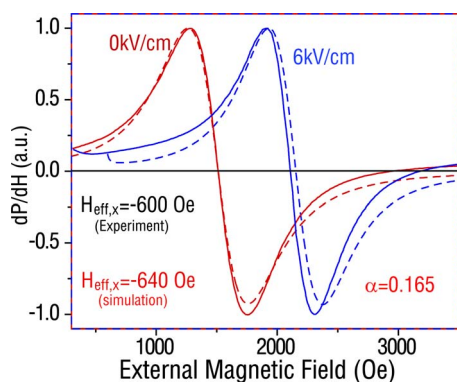


FIG. 5. (Color online) Simulated FMR spectra (dashed line) dependence of electric fields compared with experimental results (solid line).

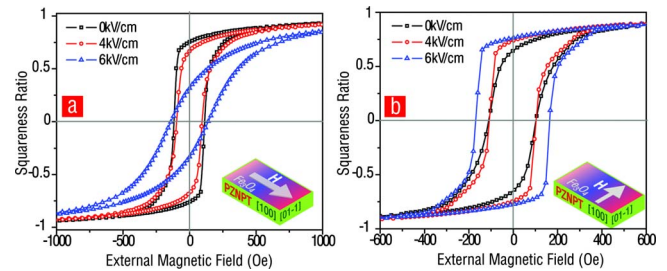


FIG. 6. (Color online) Magnetic hysteresis loop changes while external magnetic fields are along [100] and [011] direction of $\text{Fe}_3\text{O}_4/\text{PZN-PT}$.

Oe cm/kV, respectively. In addition, a high electric field tunable field of 960 Oe was obtained when the external magnetic field was switched 90° . The $\text{Fe}_3\text{O}_4/\text{PMN-PT}$ multiferroic heterostructures with strong ME coupling at microwave frequencies provide great potentials for electrostatically tunable multifunctional multiferroic device applications.

ACKNOWLEDGMENTS

This work is financially supported by NSF awards (Award Nos. 0746810 and 0603115) and ONR awards (Award Nos. N000140710761 and 000140810526).

- ¹J. F. Scott, *Nature Mater.* **6**, 256 (2007).
- ²M. Fiebig, *J. Phys. D* **38**, R123 (2005).
- ³C. W. Nan, M. I. Bichurin, S. X. Dong, and D. Viehland, *J. Appl. Phys.* **103**, 031101 (2008).
- ⁴J. Zhai, Z. Xing, S. X. Dong, J. F. Li, and D. Viehland, *Appl. Phys. Lett.* **88**, 062510 (2006).
- ⁵H. Zheng, J. Wang, S. E. Lofland, Z. Ma, L. Mohaddes-Ardabili, T. Zhao, L. Salamanca-Riba, S. R. Shinde, S. B. Ogale, F. Bai, D. Viehland, Y. Jia, D. G. Schlom, M. Wuttig, A. Roytburd, and R. Ramesh, *Science* **303**, 661 (2004).
- ⁶M. Liu, X. Li, H. Imrane, Y. Chen, T. Goodrich, K. S. Ziemer, J. Y. Huang, and N. X. Sun, *Appl. Phys. Lett.* **90**, 152501 (2007).
- ⁷Y. H. Chu, L. W. Martin, M. B. Holcomb, M. Gajek, S. Han, Q. He, N. Balke, C. Yang, D. Lee, W. Hu, Q. Zhan, P. Yang, A. Fraile-Rodriguez, A. Scholl, S. X. Wang, and R. Ramesh, *Nature Mater.* **7**, 478 (2008).
- ⁸Y. K. Fetisov and G. Srinivasana, *Appl. Phys. Lett.* **88**, 143503 (2006).
- ⁹C. Pettiford, J. Lou, L. Russell, and N. X. Sun, *Appl. Phys. Lett.* **92**, 122506 (2008).
- ¹⁰S. X. Dong, J. Zhai, J. Li, D. Viehland, and E. Summers, *J. Appl. Phys.* **101**, 124102 (2007).
- ¹¹A. Ustinov, G. Srinivasan, and B. A. Kalinikos, *Appl. Phys. Lett.* **90**, 031913 (2007).
- ¹²V. M. Petrov, G. Srinivasan, M. I. Bichurin, and A. Gupta, *Phys. Rev. B* **75**, 224407 (2007).
- ¹³J. Lou, M. Liu, D. Reed, Y. Ren, and N. X. Sun, *Adv. Mater.* **21**, 4711 (2009).
- ¹⁴M. Liu, O. Obi, J. Lou, S. Stoute, J. Y. Huang, Z. Cai, K. S. Ziemer, and N. X. Sun, *Appl. Phys. Lett.* **92**, 152504 (2008).
- ¹⁵S. X. Dong, J. Zhai, Z. Xing, J. Li, and D. Viehland, *Appl. Phys. Lett.* **91**, 022915 (2007).
- ¹⁶A. S. Tatarenko, V. Gheevarghese, and G. Srinivasan, *Electron. Lett.* **42**, 540 (2006).
- ¹⁷J. Lou, D. Reed, M. Liu, and N. X. Sun, *Appl. Phys. Lett.* **94**, 112508 (2009).
- ¹⁸M. Liu, O. Obi, J. Lou, S. Stoute, Z. Cai, K. S. Ziemer, and N. X. Sun, *J. Phys. D* **42**, 045007 (2009).
- ¹⁹S. Shastry, G. Srinivasan, M. I. Bichurin, V. M. Petrov, and A. S. Tatarenko, *Phys. Rev. B* **70**, 064416 (2004).
- ²⁰J. Das, Y. Song, N. Mo, P. Krivosik, and C. E. Patton, *Adv. Mater.* **21**, 2045 (2009).

- ²¹J. Lou, D. Reed, C. Pettiford, M. Liu, P. Han, S. X. Dong, and N. X. Sun, [Appl. Phys. Lett.](#) **92**, 262502 (2008).
- ²²M. Liu, O. Obi, J. Lou, Y. Chen, Z. Cai, S. Stoute, M. Espanol, M. Lew, X. Situ, K. S. Ziemer, V. G. Harris, and N. X. Sun, [Adv. Funct. Mater.](#) **19**, 1826 (2009).
- ²³M. Levy, H. E. Bass, and R. R. Stern, *Handbook of Elastic Properties of Solides Liquids, and Gases* (Academic, New York, 2001), Vol. 2.
- ²⁴N. X. Sun, S. X. Wang, T. J. Silva, and A. B. Kos, [IEEE Trans. Magn.](#) **38**, 146 (2002).